Self-redox reaction driven in situ formation of $Cu_2O/Ti_3C_2T_x$ nanosheets boost the photocatalytic eradication of multi-drug resistant bacteria from infected wound

Ya-Ju Hsu[1†], Amit Nain[1†], Yu-Feng Lin[1], Yu-Ting Tseng[1], Yu-Jia Li[1], Arumugam Sangili[1], Pavitra Srivastava[2], Hui-Ling Yu[1], Yu-Fen Huang[3], Chih-Ching Huang[4,5*] and Huan-Tsung Chang[1*]

Abstract

Background: MXenes with interesting optical and electrical properties have been attractive in biomedical applications such as antibacterial and anticancer agents, but their low photogeneration efficiency of reactive oxygen species (ROS) and poor stability are major concerns against microbial resistance.

Methods: Water-dispersible single layer $Ti_3C_2T_x$-based MXene through etching tightly stacked MAX phase precursor using a minimally intensive layer delamination method. After addition of Cu(II) ions, the adsorbed Cu(II) ions underwent self-redox reactions with the surface oxygenated moieties of MXene, leading to in situ formation of Cu_2O species to yield $Cu_2O/Ti_3C_2T_x$ nanosheets (heterostructures).

Results: Under NIR irradiation, the Cu_2O enhanced generation of electron–hole pairs, which boosted the photocatalytic production of superoxide and subsequent transformation into hydrogen peroxide. Broad-spectrum antimicrobial performance of $Cu_2O/Ti_3C_2T_x$ nanosheets with sharp edges is attributed to the direct contact-induced membrane disruption, localized photothermal therapy, and in situ generated cytotoxic free radicals. The minimum inhibitory concentration of $Cu_2O/Ti_3C_2T_x$ nanosheets reduced at least tenfold upon NIR laser irradiation compared to pristine $Cu_2O/Ti_3C_2T_x$ nanosheets. The $Cu_2O/Ti_3C_2T_x$ nanosheets were topically administrated on the methicillin-resistant *Staphylococcus aureus* (MRSA) infected wounds on diabetic mice.

Conclusion: Upon NIR illumination, $Cu_2O/Ti_3C_2T_x$ nanosheets eradicated MRSA and their associated biofilm to promote wound healing. The $Cu_2O/Ti_3C_2T_x$ nanosheets with superior catalytic and photothermal properties have a great scope as an effective antimicrobial modality for the treatment of infected wounds.

Keywords: MXene, Cuprous oxide, Photoresponsive nanomaterials, Antimicrobials, Wound healing

†Ya-Ju Hsu and Amit Nain contributed equally to this work

*Correspondence: huanging@ntou.edu.tw; changht@ntu.edu.tw

[1] Department of Chemistry, National Taiwan University, Taipei 10617, Taiwan
[4] Department of Bioscience and Biotechnology and Center of Excellence for the Oceans, National Taiwan Ocean University, Keelung 202301, Taiwan
Full list of author information is available at the end of the article

Hsu *et al. Journal of Nanobiotechnology*   (2022) 20:235

Page 2 of 15

Graphical Abstract
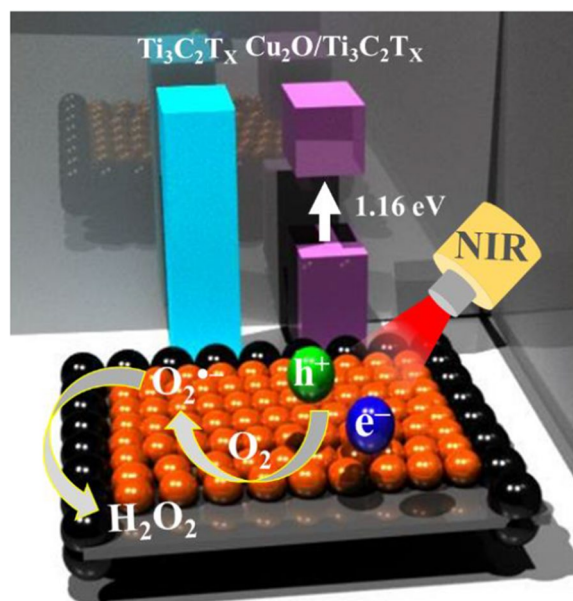
Background

Infectious diseases pose a serious threat to humankind and global economy [1]. Antimicrobial resistance (AMR), gave rise to the situation of global health emergency [2]. Once bacteria come in contact with an exposed wound, they consume nutrients from surrounding and initiate the formation of biofilm at an alarming rate, which is much faster in diabetic patients [3]. Conventional antibiotics such as streptomycin and vancomycin combat bacterial infections by causing irreparable damage to the bacteria through various mechanisms like inhibition of essential proteins [4]. Antibiotics not only treat microbial infections but also play an indispensable role in preventing severe infections in chronically ill patients such as diabetes and renal disease or who have had complex surgeries [5, 6]. Emergence of AMR along with massive reports of overdose or misuse of administered antibiotics are responsible for impotency of existing antibiotics [7]. From the year of 2050, microbial infections will account for the death of more than 10 million people per year [8]. Moreover, multidrug resistance (MDR) bacteria can produce enzymes to degrade or inactivate antibiotics, or to alter bacterial efflux pumps, targeting binding sites, and entry ports to inhibit antibiotics [9]. With the deteriorating efficiency of currently available antibiotics and growing AMR, it is of great importance to discover alternative strategies against infectious diseases.

To circumvent the challenges associated with AMR, various carbon-, metal/metal oxide-, and two-dimensional (2D) nanomaterial-based antimicrobial modalities have been developed to disintegrate bacteria via complex mechanisms, including disruption of bacterial membranes, proteolysis, degradation of DNA, or elevated oxidative stress [10–13]. Owing to their small sizes, large surface area, and mechanical strength, these particles can strongly and directly contact with bacterium membranes to achieve desirable antimicrobial activities [14–16]. These nanomaterials that are often recognized as "endogenous antimicrobial" can delay bacterial damage, and thus repeated administration inevitably leads to AMR [17]. In addition, cytotoxicity of metal ions leached out from nanoparticle surfaces is also a concern [18]. Although surface passivation is feasible using small organic ligands, polymers, and biomacromolecules, antibacterial activity is compromised [19]. Therefore, development of biocompatible nanomaterials that offer multiple routes of biocidal action in vivo systems or clinical settings is a colossal challenge.

Ultrathin 2D nanomaterials with the lateral size larger than 100 nm and thickness of only a single- or few-atoms thick (< 5 nm) represent an emerging class of antimicrobials, mainly due to their huge specific surface and faster electron transfer ensuring sufficient surface-active sites [20–22]. For example, Zhao et al. reported highly

Hsu *et al. Journal of Nanobiotechnology*   (2022) 20:235

Page 3 of 15

catalytic reduced graphene oxide nanosheets for antimicrobial therapies [23]. The nanosheets provided therapeutic potency against MDR bacteria; however, they were non-responsive to near-infrared (NIR) irradiation, and thus they do not allow in-depth tissue penetration and generation of localized heat (>50 °C) to inactivate the bacteria. Another report, Ding et al. showed the synthesis of CuS/graphitic carbon nitride (g-C3N4) heterojunctions for NIR-laser irradiation-assisted photothermal therapy [24]. Although the heterojunctions induced faster electron transfer to promote photocatalytic performance, they could not generate H_2O_2.

Currently, MXene is a fast-growing family of 2D materials, comprised of transition metal carbides, carbonitride, and nitrides with a general formula of $M_{n+1}X_nT_x$, where M is an early transition metal (e.g., Sc, Ti, V, Cr, Zr, Nb, Mo, Hf), X is carbon and/or nitrogen, and T_x is a surface terminal group (−F, −OH, −O, etc.) [25–27]. Owing to the fascinating properties including hydrophilicity, biocompatibility, conductivity, and photothermal properties, MXene has shown potential for biomedical applications [28, 29]. Rasool and coworkers proposed that the antibacterial activity of colloidal $Ti_3C_2T_x$ nanosheets was originated from direct contact assisted oxidative stress-induced membrane disruption [30]. Size-dependent antibacterial properties of MXene have been reported; smaller ones exhibited a more substantial antimicrobial effect due to their sharp edges [31]. Recently, Li et al. demonstrated the synergistic therapy of bismuth sulfide/titanium carbide MXene ($Bi_2S_3/Ti_3C_2T_x$) heterojunctions against microbial pathogenesis, which resulted in rapid wound healing [32]. Nanocomposites extensively improved the photocatalytic generation of reactive oxygen species (ROS), due to formation of Schottky-type defects, which suppressed the recombination of NIR (808 nm)-induced electron–hole pairs. Work function-dependent interfacial engineering of $Ti_3C_2T_x$ MXene significantly boosted the photocatalytic therapeutic action, but only against planktonic cells. In addition, most antimicrobial activities of MXene were shown in aqueous solutions with low ionic strength, mainly because of its poor stability in biologically complex fluids [33].
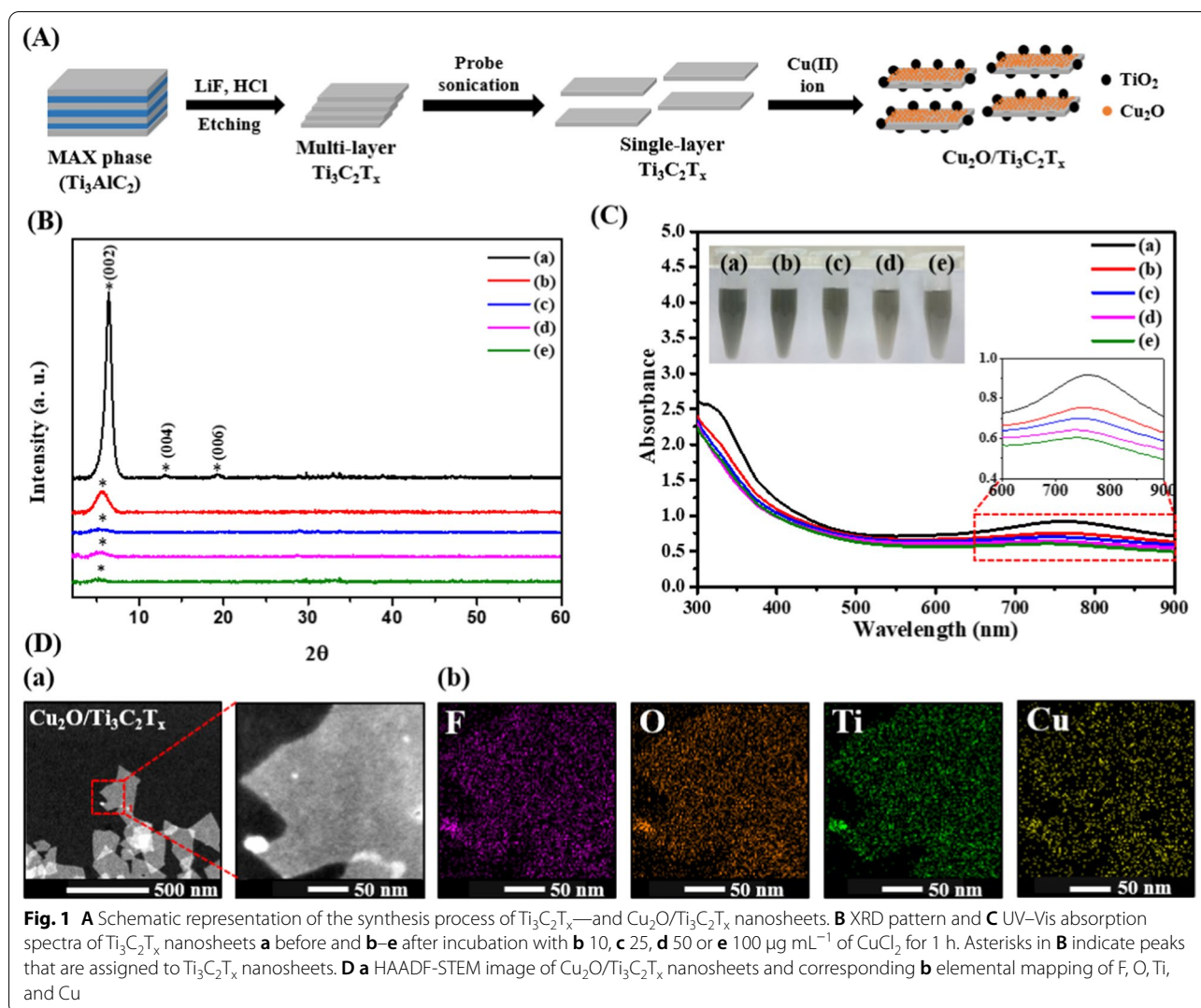
In this work, we prepared highly stable and aqueous dispersible single layer $Ti_3C_2T_x$ MXene nanosheets via layer delamination and subsequent etching of the MAX precursor. After addition of Cu(II) ions, they were adsorbed onto the negatively charged and oxygenated surface of $Ti_3C_2T_x$ MXene nanosheets and subsequently induced in situ formation of titanium dioxide (TiO_2) and cuprous oxide (Cu_2O) species through their redox reactions to yield $Cu_2O/Ti_3C_2T_x$ MXene nanosheets (heterostructures) (Fig. 1A). The $Ti_3C_2T_x$ MXene nanosheets photogenerated electron–hole pairs upon NIR (650–850 nm) irradiation, meanwhile the surface Cu_2O species boosted the production of superoxide ($O_2^{•-}$) radicals and subsequent transformation of them into hydrogen peroxide (H_2O_2). As-prepared $Cu_2O/Ti_3C_2T_x$ MXene nanosheets displayed broad-spectrum antimicrobial susceptibility, including MDR bacteria. Localized heating and cytotoxic reactive oxygen species are responsible for its superior antibacterial activity. In addition, the direct contact also caused irreparable membrane damage due to the sharp edges of nanosheets. The $Cu_2O/Ti_3C_2T_x$ Mxene nanosheets showed insignificant cytotoxicity and hemolytic activity against human skin cells (NIH-3T3 skin cells) and erythrocytes, respectively. The practicality of $Cu_2O/Ti_3C_2T_x$ Mxene nanosheets was demonstrated by curing diabetic mice with superficial wounds infected with methicillin-resistant *Staphylococcus aureus* (MRSA). Under photoirradiation, $Cu_2O/Ti_3C_2T_x$ MXene nanosheets eliminated microbial pathogenesis and promoted wound healing via angiogenesis, epithelialization, and collagen deposition.

Results

In situ formation of Cu_2O on $Ti_3C_2T_x$ MXene nanosheets

Rough surfaces of tightly stacked Ti_3AlC_2 flakes (i.e., commercially purchased MAX phase; Additional file 1: Fig. S1A) were etched with a freshly prepared mixture of hydrofluoric acid and lithium fluoride to remove aluminum to yield multilayer $Ti_3C_2T_x$ nanosheets (i.e., MXene; Fig. S1B), which were then subjected to sonication to form well-dispersed single or few layers of $Ti_3C_2T_x$ MXene nanosheets (Fig. S1C) [34]. Selected area electron diffraction (SAED) analysis revealed a distinct (002) plane of hexagonal $Ti_3C_2T_x$ nanosheets (Additional file 1: Fig. S2A) [35]. The X-ray diffraction (XRD) pattern of $Ti_3C_2T_x$ nanosheets exhibits a characteristic peak centered at 6.3° ascribing to (002) basal plane of MXene (Fig. 1B) [36]. The MXene nanosheets were further incubated with $CuCl_2$ at an ambient temperature for 1 h to deposit Cu(II) ions onto $Ti_3C_2T_x$ nanosheets (Fig. 1A). The XRD pattern (Fig. 1B) shows a gradual decrease in the signal intensity of (002) plane upon increasing Cu(II) concentration, indicating disruption of the crystal structure probably due to in situ self-oxidation of MXene to form Cu_2O and TiO_2 species [37]. The X-ray photoelectron spectroscopy (XPS) analysis of $Ti_3C_2T_x$ MXene (17.2%/47.0%/21.2%) shows that relative abundance of $Ti^+/Ti^{2+}/Ti^{3+}$ is significantly reduced after Cu deposition (Additional file 1: Fig. S3A), whereas Ti^{4+} (i.e., TiO_2) is greatly increased [38]. The XPS spectra show characteristic peaks of Cu $2p_{1/2}$ and Cu $2p_{3/2}$ at 932.5 and 952.3 eV (Additional file 1: Fig. S3B), respectively, attributed to the presence of Cu_2O species, supporting that the deposited Cu(II) ions reacted with oxygenated moieties on the surface of $Ti_3C_2T_x$ MXene to
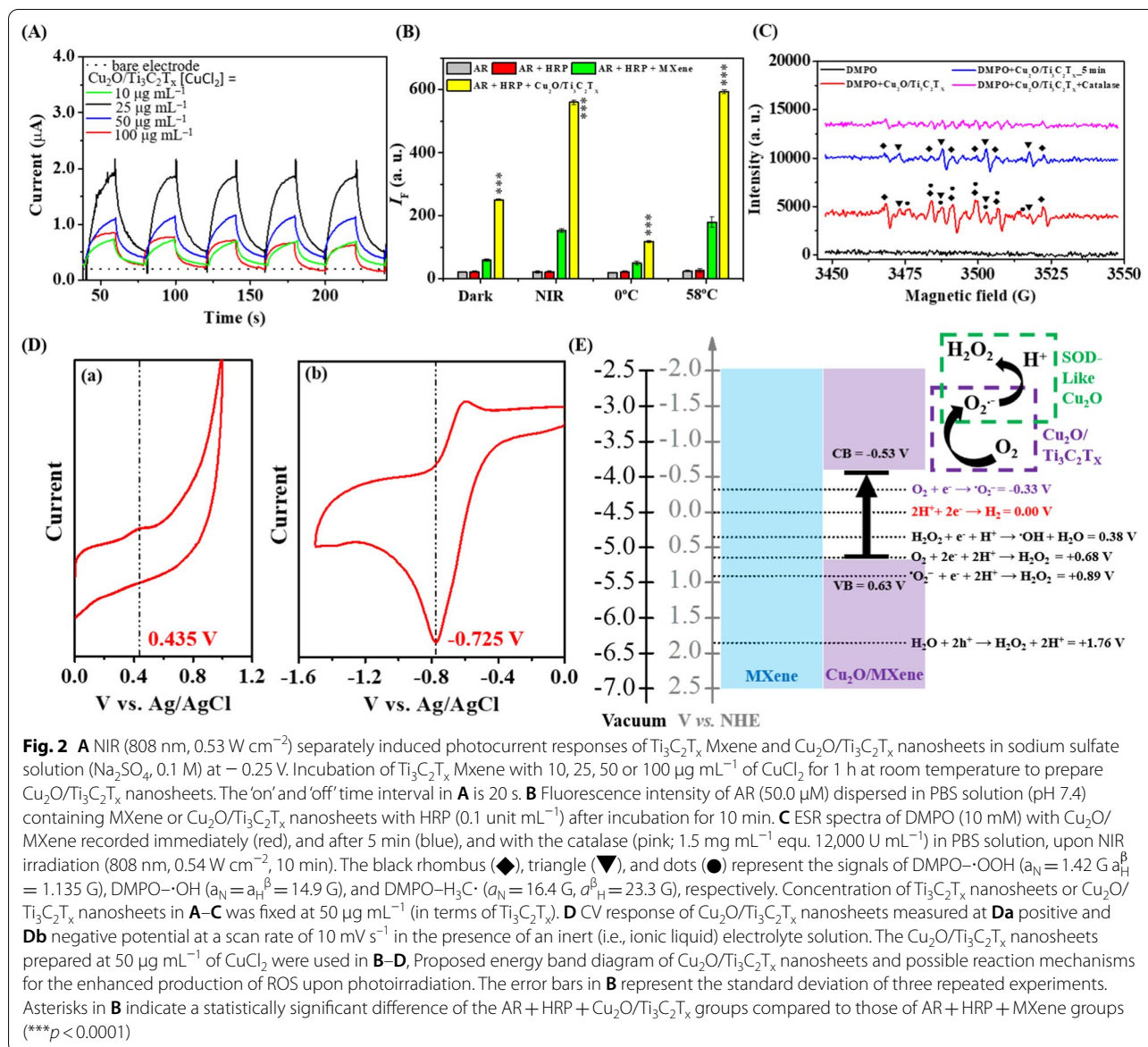
Hsu *et al. Journal of Nanobiotechnology*   (2022) 20:235

Page 4 of 15

Fig. 1 **A** Schematic representation of the synthesis process of $Ti_3C_2T_x$—and $Cu_2O/Ti_3C_2T_x$ nanosheets. **B** XRD pattern and **C** UV–Vis absorption spectra of $Ti_3C_2T_x$ nanosheets **a** before and **b**–**e** after incubation with **b** 10, **c** 25, **d** 50 or **e** 100 μg mL^{-1} of $CuCl_2$ for 1 h. Asterisks in **B** indicate peaks that are assigned to $Ti_3C_2T_x$ nanosheets. **D a** HAADF-STEM image of $Cu_2O/Ti_3C_2T_x$ nanosheets and corresponding **b** elemental mapping of F, O, Ti, and Cu

transform into Cu_2O to yield $Cu_2O/Ti_3C_2T_x$ nanosheets (heterostructures) through self-induced redox reactions [39]. No obvious characteristic diffraction peaks of as-formed TiO_2 and Cu_2O suggest that they are present on MXene in amorphous forms.

Transmission electron microscope (TEM), scanning electron microscope (SEM) and atomic force microscopy (AFM) show $Cu_2O/Ti_3C_2T_x$ nanosheets have an average size and thickness of ca. 200 and 1.84 nm, along with rough edges due to in situ formation of Cu_2O and TiO_2 species (Additional file 1: Figs. S4 and S5). Their UV–Visible absorption spectroscopy results are in good agreement with the XRD and XPS analysis, displaying the well-known characteristic wide range near-infrared (NIR) band (650–850 nm) of $Ti_3C_2T_x$ MXene (Fig. 1C) apparently decreases upon increasing Cu(II) concentration mainly because of the self-oxidation induced structural disruption of $Ti_3C_2T_x$ MXene (inset to Fig. 1C) [40].

The high-angle annular dark-field scanning transmission electron microscopy (HAADF-STEM; Fig. 1Da) coupled with energy-dispersive X-ray spectroscopy (EDX) elemental mapping indicates the coexistence of Ti, F, Cu, and O in $Cu_2O/Ti_3C_2T_x$ heterostructures and the bigger sized TiO_2 NPs are formed on the edges of nanosheets (Fig. 1Db).

Generation of $O_2^{\bullet-}/H_2O_2$ by $Cu_2O/Ti_3C_2T_x$ heterostructures
First, we demonstrated the capacity of $Cu_2O/Ti_3C_2T_x$ nanosheets to generate NIR-induced electron−hole pairs (Fig. 2A) [41]. $Ti_3C_2T_x$ MXene could not generate photocurrent due to their intrinsic metallic/metal-like behavior upon NIR irradiation (808 nm, 0.53 W cm^{-2}) [42]. On the other hand, $Cu_2O/Ti_3C_2T_x$ nanocomposites showed obvious photocurrent responses as compared to a bare electrode, mainly due to the formation of semiconducting Cu_2O on the surface of nanosheets. The photocurrent

Hsu *et al. Journal of Nanobiotechnology*   (2022) 20:235

Page 5 of 15

Fig. 2 A NIR (808 nm, 0.53 W cm^{-2}) separately induced photocurrent responses of Ti$_3$C$_2$T$_x$ Mxene and Cu$_2$O/Ti$_3$C$_2$T$_x$ nanosheets in sodium sulfate solution (Na$_2$SO$_4$, 0.1 M) at − 0.25 V. Incubation of Ti$_3$C$_2$T$_x$ Mxene with 10, 25, 50 or 100 μg mL^{-1} of CuCl$_2$ for 1 h at room temperature to prepare Cu$_2$O/Ti$_3$C$_2$T$_x$ nanosheets. The 'on' and 'off' time interval in **A** is 20 s. **B** Fluorescence intensity of AR (50.0 μM) dispersed in PBS solution (pH 7.4) containing MXene or Cu$_2$O/Ti$_3$C$_2$T$_x$ nanosheets with HRP (0.1 unit mL^{-1}) after incubation for 10 min. **C** ESR spectra of DMPO (10 mM) with Cu$_2$O/MXene recorded immediately (red), and after 5 min (blue), and with the catalase (pink; 1.5 mg mL^{-1} equ. 12,000 U mL^{-1}) in PBS solution, upon NIR irradiation (808 nm, 0.54 W cm^{-2}, 10 min). The black rhombus (◆), triangle (▼), and dots (●) represent the signals of DMPO–·OOH (a_N = 1.42 G a_H^β = 1.135 G), DMPO–·OH ($a_N = a_H^\beta$ = 14.9 G), and DMPO–H$_3$C· (a_N = 16.4 G, a_H^β = 23.3 G), respectively. Concentration of Ti$_3$C$_2$T$_x$ nanosheets or Cu$_2$O/Ti$_3$C$_2$T$_x$ nanosheets in **A**–**C** was fixed at 50 μg mL^{-1} (in terms of Ti$_3$C$_2$T$_x$). **D** CV response of Cu$_2$O/Ti$_3$C$_2$T$_x$ nanosheets measured at **Da** positive and **Db** negative potential at a scan rate of 10 mV s^{-1} in the presence of an inert (i.e., ionic liquid) electrolyte solution. The Cu$_2$O/Ti$_3$C$_2$T$_x$ nanosheets prepared at 50 μg mL^{-1} of CuCl$_2$ were used in **B**–**D**, Proposed energy band diagram of Cu$_2$O/Ti$_3$C$_2$T$_x$ nanosheets and possible reaction mechanisms for the enhanced production of ROS upon photoirradiation. The error bars in **B** represent the standard deviation of three repeated experiments. Asterisks in **B** indicate a statistically significant difference of the AR + HRP + Cu$_2$O/Ti$_3$C$_2$T$_x$ groups compared to those of AR + HRP + MXene groups (***p < 0.0001)

(~ 1.83 × 10^{-6} A) produced by the Cu$_2$O/Ti$_3$C$_2$T$_x$ nanosheets ([Cu(II)] = 25 μg mL^{-1}) is at least 2.4-fold higher than those (7.75 × 10^{-7} A) nanosheets prepared using 10 μg mL^{-1} of Cu(II), suggesting that amplified photocurrent response of Cu$_2$O/Ti$_3$C$_2$T$_x$ is attributed to the formation of heterostructures formed by the coupling of Cu$_2$O with TiO$_2$/Ti$_3$C$_2$T$_x$ [43]. Further increase in Cu(II) concentration i.e., 50 or 100 μg mL^{-1} (in terms of Cu) resulted in a significant drop in the photocurrent, probably due to higher degree oxidation of Ti$_3$C$_2$T$_x$ MXene (TiO$_2$ > 94%, Additional file 1: Fig. S2). The presence of Cu$_2$O in crystalline Ti$_3$C$_2$T$_x$ nanosheets created an energy barrier (i.e., Schottky junction), which restricted the electron–hole pair recombination and facilitated the faster

transfer of photogenerated electrons to the surface, leading to the enhanced photocurrent response [44]. Due to the substantial photoactivity through modulating electrons-holes, we further investigated the catalytic formation of hydrogen peroxide (H$_2$O$_2$) under NIR irradiation. Efficient generation of H$_2$O$_2$ was demonstrated through a combination of Amplex Red (AR) and horseradish peroxidase (HRP) assays [45]. HRP decomposes H$_2$O$_2$ to facilitate an electron transfer induced AR-oxidation to yield a highly fluorescent product resorufin (7-hydroxy-3H-phenoxazin-3-one; quantum yield: 0.83) [46]. As-prepared Cu$_2$O/Ti$_3$C$_2$T$_x$ heterostructures generated a comparable amount of H$_2$O$_2$ (10 μM), which is ~ fivefold higher than that of the Ti$_3$C$_2$T$_x$ MXene at an ambient

Hsu *et al. Journal of Nanobiotechnology*   (2022) 20:235

Page 6 of 15

temperature under dark condition (Fig. 2B). Interestingly, the amount of H_2O_2 generated by $Cu_2O/Ti_3C_2T_x$ was further improved twofold when coupled with NIR irradiation (808 nm, 0.54 W cm^{-2}, 10 min). In control experiments, reaction carried at 58 $^{\circ}$C (equivalent to the NIR induced temperature) with $Cu_2O/Ti_3C_2T_x$ nanosheets revealed a similar trend to that of NIR laser, indicating that spontaneous formation of H_2O_2 can be ascribed to the NIR induced in situ thermal gradients (Fig. 2B) [47].

The electron spin resonance (ESR) spectra of $Cu_2O/Ti_3C_2T_x$ heterostructures using 5,5-dimethyl-1pyrroline-N-oxide (DMPO) as a spin trap exhibited mixture of signals, corresponding to hydroxyl ($\cdot$OH) and hydroperoxyl/superoxide ($\cdot$OOH/$O_2^{\bullet-}$) (Fig. 2C) [48]. In addition, a weak signal corresponding to methyl radical ($H_3C\cdot$) was also observed, ascribing to the copper-induced oxidation of DMPO. Upon incubation at an ambient temperature for 5 min, the peak for $\cdot$OH quartet (1:2:2:1) became more intense, and disappeared in the presence of catalase, suggesting the $\cdot$OH originated from H_2O_2 (Fig. 2C) [49]. Nevertheless, the ESR spectra show weak intensity sextet ascribing to $\cdot$OOH/$O_2^{\bullet-}$ in the absence of NIR, under parallel conditions (Additional file 1: Fig. S6). Control group (only Cu(II)) did not reveal any obvious peak after incubating with DMPO in the absence or presence of NIR (data not shown). To confirm the formation of $O_2^{\bullet-}$ as an intermediate for subsequent formation of H_2O_2, we employed a tetrazolium dye MTT [3-(4,5-dimethyl-thiazol-2-yl) 2,5-diphenyl tetrazolium bromide] reduction method to form it's colored formazan, as reported previously [50]. Additional file 1: Fig. S7 indicates that $Cu_2O/Ti_3C_2T_x$ ($Abs_{576} \sim 0.22$) produced at least fourfold higher $O_2^{\bullet-}$ as compared to the control ($Abs_{576} \sim 0.05$) without NIR irradiation, which is consistent with the low-intensity ESR peaks shown in Additional file 1: Fig. S6. In addition, spontaneous production of $O_2^{\bullet-}$ was further improved threefold under NIR irradiation ($Abs_{576} \sim 0.61$), which is comparable to that provided by potassium dioxide (positive control; 0.5 mg mL^{-1}).

2D structures with ultrafast charge carriers, huge surface area for redox reactions, broad-band absorption profile, and presence of heteroatom are the features of a modern photocatalyst [51]. Electrochemical behaviors of $Cu_2O/Ti_3C_2T_x$ heterostructures were studied by cyclic voltammetry (CV). The CV curves in a wide potential window were recorded to determine the position of valence band (VB; Fig. 2Da) and conduction band (CB; Fig. 2Db) [52, 53]. The energy band gap (E_g) was calculated as 1.16 eV using Eq. (3):

$$E_{VB}(eV) = -\left(E_{oxidation}\ vs\ Ag/AgCl + 0.197 + 4.74\right) \tag{1}$$

$$E_{CB}(eV) = -\left(E_{reduction}\ vs\ Ag/AgCl + 0.197 + 4.74\right) \tag{2}$$

$$E_g = E_{CB} - E_{VB} \tag{3}$$

As shown in Fig. 2E, $Cu_2O/Ti_3C_2T_x$ nanosheets can promote the thermodynamically favorable formation of $O_2^{\bullet-}$ ($O_2 + e^- \rightarrow O_2^{\bullet-}$ $E^0 = -0.33$ V) upon NIR illumination, which were subsequently converted into H_2O_2 ($O_2^{\bullet-} + e^- + 2H^+ \rightarrow H_2O_2$ $E^0 = +0.89$ V) by superoxide dismutase-like Cu_2O species on the MXene surface [54]. Improved photoresponse of the $Cu_2O/Ti_3C_2T_x$ for the production of $O_2^{\bullet-}$ is attributed to the formation of heterostructures that facilitated fast electron transfer and created catalytically active reaction centers with higher surface energy at the lattice heterojunctions between Cu_2O and crystal facets of $Ti_3C_2T_x$ in the nanosheets (Fig. 2E) [55]. Although the possibility of Fenton-like reaction of Cu(II)/Cu(I) for the generation of $\cdot$OH/H_2O_2 cannot be ruled out, we believe that the $Cu_2O/Ti_3C_2T_x$ heterostructures effectively inhibited the electron–hole pair recombination by creating an energy barrier, which promoted interfacial charge transfer for the generation of $O_2^{\bullet-}$ [55].

Photothermal effects of $Cu_2O/Ti_3C_2T_x$ heterostructures

We further investigated the photothermal properties of MXene and $Cu_2O/MXene$ nanosheets. Temperature profiles of aqueous solution in the absence (control; PBS) and presence of 50 μg mL^{-1} (in terms of Ti_3C_{2Tx}) of MXene or $Cu_2O/MXene$ nanosheets under continuous NIR laser irradiation (808 nm, 0.54 W cm^{-2}) for 10 min are separately shown in Fig. 3A. As compared to PBS ($\sim$ 38 $^{\circ}$C), both $Ti_3C_2T_x$ MXene and $Cu_2O/MXene$ exhibited significant increases in temperature (> 57 $^{\circ}$C) up to 300 s as a result of high light-harvesting ability and strong localized surface plasmon resonance (LSPR) effects [56]. The $Ti_3C_2T_x$ nanosheets exhibited a characteristic SPR ascribed to the presence of the (002) crystal planes of $Ti_3C_2T_x$, and the mobility of free charge carriers across the plane due to NIR irradiation that are indeed consistent with the natural specific frequency of plasmonic $Ti_3C_2T_x$, as a result of the higher photothermal effects [56]. Both $Ti_3C_2T_x$ MXene and $Cu_2O/MXene$ nanosheets showed obvious power density- and concentration-dependent temperature elevation profiles (Additional file 1: Fig. S8). The photothermal conversion efficiency (η) values of $Ti_3C_2T_x$ and $Cu_2O/Ti_3C_2T_x$ nanosheets were determined by applying a slightly modified reported method to be ca. 53% and 49%, respectively (Additional file 1: Fig. S9) [57], which are comparable to or better than previous reports on MXene structures [58, 59]. Upon NIR laser irradiation, the oscillating electromagnetic field generated from the illuminated low-energy photons excites the free electrons of $Ti_3C_2T_x$ nanosheets
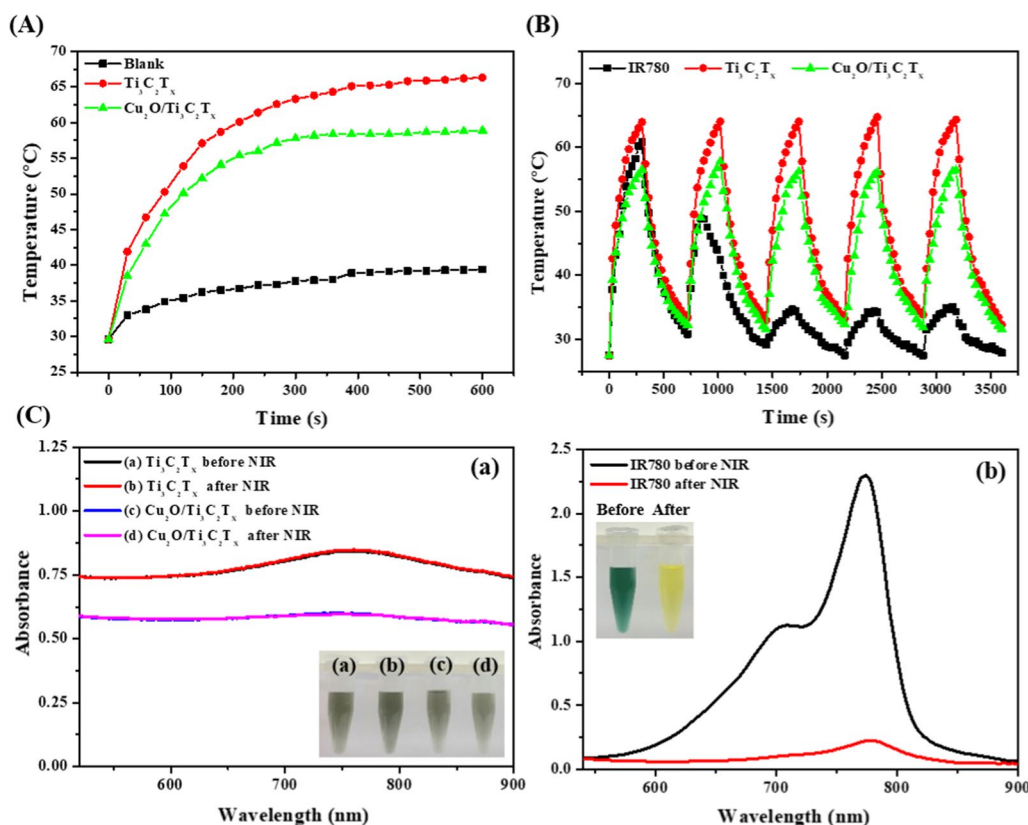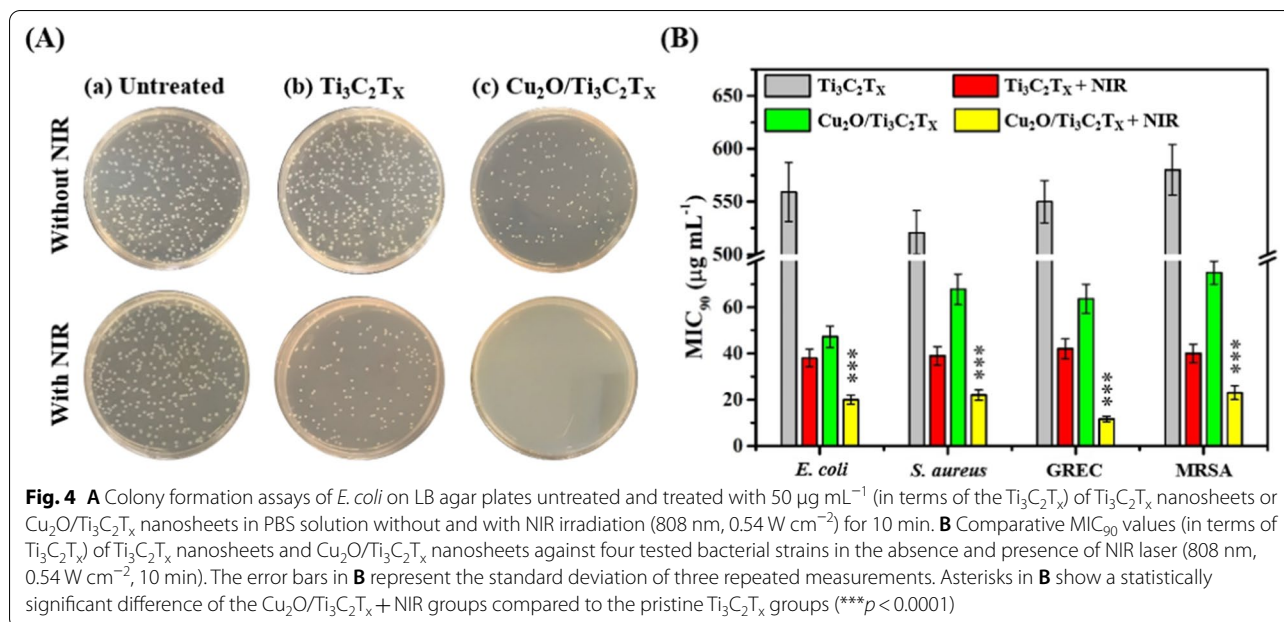
Fig. 3 **A** Temperature profiles of $Ti_3C_2T_x$ nanosheets and $Cu_2O/Ti_3C_2T_x$ nanosheets under NIR laser irradiation (808 nm, 0.54 W cm^{-2}). **B** Thermal responses of $Ti_3C_2T_x$ nanosheets, $Cu_2O/Ti_3C_2T_x$ nanosheets, and IR780 iodide dye (0.1 mM) dispersed in PBS solution under NIR laser irradiation for five consecutive switch on–off cycles. **C** UV–Vis absorption spectra of the corresponding solutions before and after five consecutive "on" and "off" cycles of NIR laser irradiation. Concentrations of $Ti_3C_2T_x$ nanosheets and $Cu_2O/Ti_3C_2T_x$ nanosheets in **B** and **C** were both fixed at 50 µg mL^{-1} (in terms of $Ti_3C_2T_x$). Inset to **C** shows the photographs of corresponding solutions

to coherently and collectively oscillate in their respective vibrational energy states [60, 61]. Then, the transitions within vibrational energy level allowed multiple collisions among the excited electrons, increasing the kinetic energy of each associated electron and then elevating the system temperature [62, 63]. In addition, relative to a commercially available photothermal agent (IR-780 dye; 0.1 mM), $Ti_3C_2T_x$ and $Cu_2O/Ti_3C_2T_x$ displayed higher photothermal stability, as no significant decline in the temperature maxima was observed even after five consecutive cycles of on−off process (Fig. 3B). Absorption spectra showed no obvious color change in the $Ti_3C_2T_x$ nanosheets and $Cu_2O/Ti_3C_2T_x$ nanosheets, while a significant photobleaching of IR-780 was observed under parallel conditions (Fig. 3C). The $Cu_2O/Ti_3C_2T_x$ nanosheets displayed considerable photo-to-heat conversion efficiency and photothermal stability, which makes them an excellent candidate for photothermal therapy applications.

Potent antimicrobial activities

Owing to their excellent intrinsic catalytic activity and photothermal performance, we further evaluated the antibacterial properties of $Cu_2O/MXene$ nanosheets (with MXene as a control) against various bacterial strains, including one non-MDR gram-negative (*E. coli*), one MDR gram-negative (Gentamicin resistant *E. coli*; GREC), one non-MDR gram-positive (*S. aureus*), and one MDR gram-positive (MRSA) bacterial strains without and with NIR laser irradiation (808 nm, 0.54 W cm^{-2}). Firstly, we demonstrated the multidrug-resistant nature of bacteria (i.e., MRSA) by examining their potency against several broad-spectrum antibiotics (Additional file 1: Fig. S10). Colony formation assay of *E. coli* untreated (230 ± 4 colony–forming units (CFUs); $n = 3$) and treated with $Ti_3C_2T_x$ nanosheets and $Cu_2O/Ti_3C_2T_x$ nanosheets revealed 221 ± 5 and 115 ± 3 CFU ($n = 3$), respectively (Fig. 4A). The as-prepared $Cu_2O/Ti_3C_2T_x$ nanosheets showed negligible CFUs when coupled with the NIR laser irradiation (808 nm, 0.54 W cm^{-2}, 10 min),

Hsu *et al. Journal of Nanobiotechnology*   (2022) 20:235

Page 8 of 15

Fig. 4 **A** Colony formation assays of *E. coli* on LB agar plates untreated and treated with 50 µg mL^{-1} (in terms of the $Ti_3C_2T_x$) of $Ti_3C_2T_X$ nanosheets or $Cu_2O/Ti_3C_2T_X$ nanosheets in PBS solution without and with NIR irradiation (808 nm, 0.54 W cm^{-2}) for 10 min. **B** Comparative MIC$_{90}$ values (in terms of $Ti_3C_2T_x$) of $Ti_3C_2T_X$ nanosheets and $Cu_2O/Ti_3C_2T_X$ nanosheets against four tested bacterial strains in the absence and presence of NIR laser (808 nm, 0.54 W cm^{-2}, 10 min). The error bars in **B** represent the standard deviation of three repeated measurements. Asterisks in **B** show a statistically significant difference of the $Cu_2O/Ti_3C_2T_x$ + NIR groups compared to the pristine $Ti_3C_2T_x$ groups (***$p < 0.0001$)

while $Ti_3C_2T_x$ nanosheets (137 ± 4 CFU, $n = 3$) exhibited much less inhibitory activity (Fig. 4A). The MIC$_{90}$ (minimal inhibitory concentration required to inhibit > 90% of the bacterial population) values were determined by a standard serial dilution method (Fig. 4B) [64]. The MIC$_{90}$ values for $Cu_2O/Ti_3C_2T_x$ nanosheets were determined to be > 47 µg mL^{-1} (in terms of $Ti_3C_2T_x$), which were ~11-fold lower than that of $Ti_3C_2T_x$ MXene (> 520 µg mL^{-1}). As expected, under NIR irradiation MIC$_{90}$ values of $Cu_2O/Ti_3C_2T_x$ were further reduced to ca. 11–23 µg mL^{-1} (in terms of $Ti_3C_2T_x$). The $Cu_2O/Ti_3C_2T_x$ demonstrated remarkably superior antimicrobial performance upon NIR illumination due to the synergistic effect from catalytic and photothermal treatment.
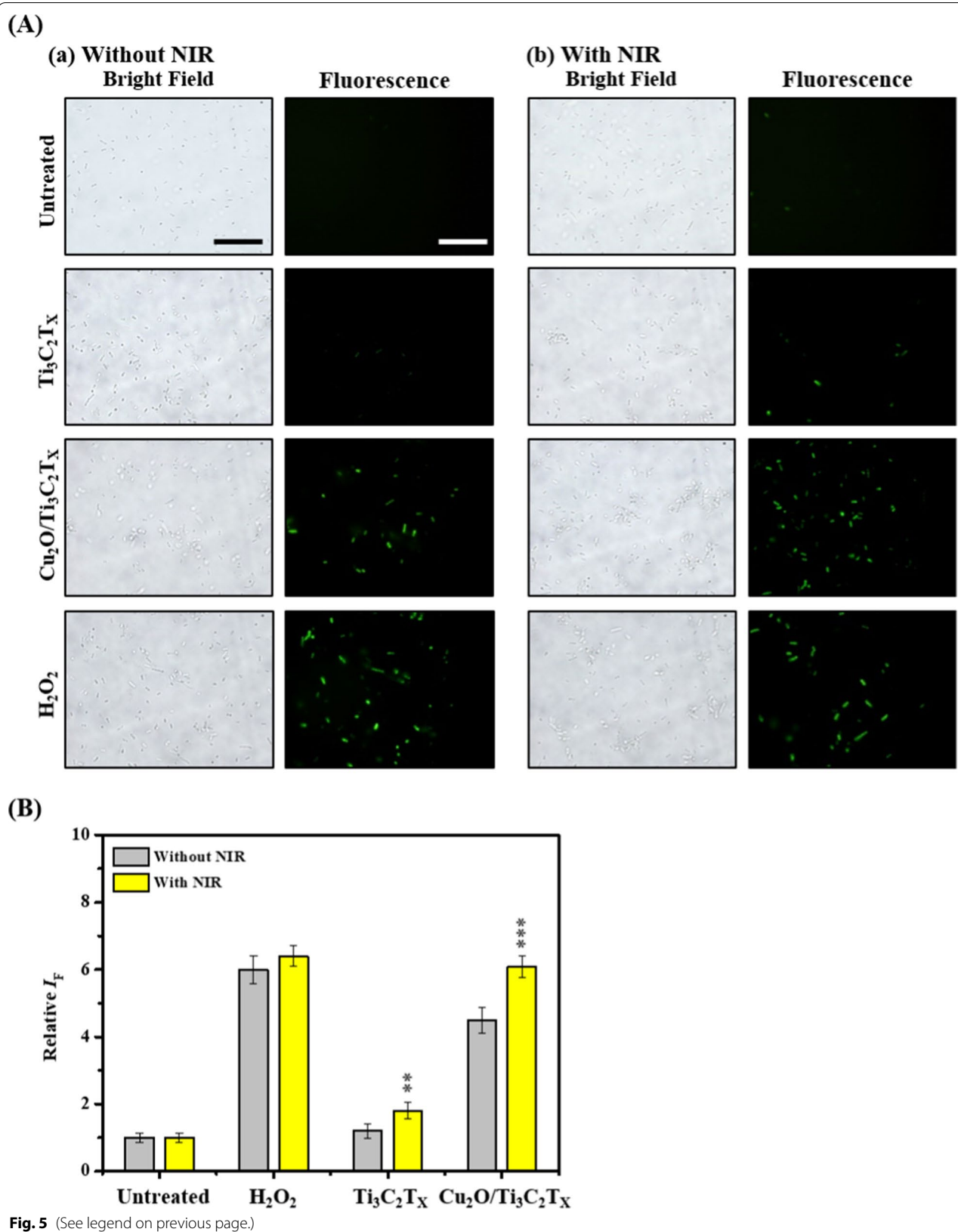
We then studied intracellular ROS production capabilities of $Ti_3C_2T_x$ and $Cu_2O/Ti_3C_2T_x$ nanosheets using the 2′,7′-dichlorodihydrofluorescein diacetate (DCFH-DA) assays [65]. We observed that *E. coli* treated with 25 µg mL^{-1} (in terms of $Ti_3C_2T_x$) of $Cu_2O/Ti_3C_2T_x$ nanosheets under NIR laser irradiation induced remarkably higher ROS levels compared to those of $Ti_3C_2T_x$ MXene or $Cu_2O/Ti_3C_2T_x$ nanosheets (without NIR irradiation) (Fig. 5). A small amount of ROS is generated in

E. coli after being treated with $Ti_3C_2T_x$ MXene with NIR laser irradiation, probably due to the photothermal effect of $Ti_3C_2T_x$ MXene induced elevation of oxidative stress in bacteria. In addition, bacterium membrane integrity in the presence of MXene or $Cu_2O/Ti_3C_2T_x$ nanosheets without and with NIR irradiation were assessed using 3,3′-dietgyloxacarbicyanine (DiOC$_2$) membrane potential staining assays (Additional file 1: Fig. S11) [66]. Suspensions of *E. coli* incubated with $Cu_2O/Ti_3C_2T_x$ nanosheets under NIR treatment showed significantly low red fluorescence intensity due to higher degree of depolarization of bacterial membranes, compared to the $Ti_3C_2T_x$ MXene or $Cu_2O/Ti_3C_2T_x$ nanosheets without photoirradiation (Additional file 1: Fig. S11B). TEM images of *E. coli* after treatment with $Cu_2O/Ti_3C_2T_x$ nanosheets (25 µg mL^{-1}) under NIR laser irradiation shows an apparently disrupted bacterial membrane, while an intact cell membrane with no obvious morphological changes was observed in untreated groups (Additional file 1: Fig. S12). The interaction of $Cu_2O/Ti_3C_2T_x$ nanosheets with the bacteria was further investigated by energy-dispersive X-ray spectroscopy (EDS) measurements of the portion of *E. coli* treated with the nanosheets, displaying a

(See figure on next page.)
Fig. 5 **A** The bright-field and fluorescence images of *E. coli* untreated and treated with 25 µg mL^{-1} (in terms of $Ti_3C_2T_x$) of $Ti_3C_2T_x$ nanosheets and $Cu_2O/Ti_3C_2T_x$ nanosheets, or H_2O_2 (20 µM) in PBS solution for 10 min without or with NIR laser irradiation (808 nm, 0.54 W cm^{-2}). **B** Microscopic images were captured after the DCFH-DA staining. **B** Relative fluorescence intensity (I_F) of DCF in *E. coli* suspensions was recorded at the excitation/emission wavelengths of 490/530 nm, respectively. The error bars in **B** represent the standard deviation of three repeated experiments. Scale bar in **A** is 10 µm. The error bars in **B** represent the standard deviation of three repeated experiments. Asterisks in **B** show statistically significant differences of the untreated, H_2O_2, $Ti_3C_2T_x$, and $Cu_2O/Ti_3C_2T_x$ groups in the presence of NIR compared to those groups treated in the absence of NIR, respectively (**$p < 0.001$, and ***$p < 0.0005$)

Hsu *et al. Journal of Nanobiotechnology*   (2022) 20:235

Page 9 of 15

Fig. 5 (See legend on previous page.)

Hsu *et al. Journal of Nanobiotechnology*   (2022) 20:235

Page 10 of 15

high-intensity signal of Cu in the surroundings (Additional file 1: Fig. S12). Superior antibacterial activity of $Cu_2O/Ti_3C_2T_x$ nanosheets coupled with NIR laser irradiation was achieved mainly due to a combined effect of catalytic and photothermal activities.

Biocompatibility of $Cu_2O/Ti_3C_2T_x$ nanocomposites

We employed the trypan blue exclusion method for determining the cell numbers and Alamarblue assays to investigate the cytotoxicity of $Cu_2O/Ti_3C_2T_x$ nanosheets against NIH-3T3 cells (CRL-1658, fibroblast cells from Swiss albino mouse embryo tissue). $Ti_3C_2T_x$ or $Cu_2O/Ti_3C_2T_x$ nanosheets exhibited insignificant cytotoxicity (< 5%) against the tested fibroblasts up to 50 μg mL^{-1} (in terms of $Ti_3C_2T_x$e), even after NIR irradiation (808 nm, 0.54 W cm^{-2}, 10 min), which is much higher than MIC$_{90}$ values of the $Cu_2O/Ti_3C_2T_x$ nanosheets. (Additional file 1: Fig. S13). ICP-MS analysis revealed that only 10% Ti and 1% Ti/2.5% Cu were leached from the surfaces of $Ti_3C_2T_x$ and $Cu_2O/Ti_3C_2T_x$ nanosheets in cell culture medium after incubated for 24 h, respectively. The modified nanosheets offered remarkable biocompatibility mainly due to their high stability, which prevented the release of metal ions in cell culture media (DMEM containing 10% FBS) in the duration of 24 h. In addition to satisfactory in vitro cytotoxicity performance, the hemolytic assay showed negligible hemolysis of erythrocytes up to 400 μg mL^{-1} (in terms of $Ti_3C_2T_x$) (Additional file 1: Fig. S14).

Effective wound healing using $Cu2O/Ti_3C_2T_x$ nanosheets coupled with NIR irradiation

Encouraged from aqueous stability, biocompatibility, and substantial antimicrobial performance in vitro, $Cu_2O/Ti_3C_2T_x$ nanosheets were applied for the treatment of infected wounds. *S. aureus* or their associated biofilms typically accounts for ca. 50% of nosocomial infection [67]. The optimal concentration of $Cu_2O/Ti_3C_2T_x$ nanosheets (50 μg mL^{-1}; in terms of $Ti_3C_2T_x$) was determined based on the results obtained from antibacterial assays (LB agar plates and MIC$_{99}$ values) as shown in Fig. 4. In addition, biocompatible assays (Additional file 1: Figs. S13 and S14) also verified the optimal concentrations. The practicality of $Cu_2O/Ti_3C_2T_x$ nanosheets was validated with the treatment of surgical wounds infected with MRSA at the back of diabetic (db/db) mice (BKS.Cg- Dock7^m+/+Lepr^{db}/J, a model of Type 2 diabetes mellitus). Figure 6Aa shows time-course photographs of the wounds untreated (PBS solution) and treated with a commercial antibacterial bandage (i.e., 3 M; containing antimicrobial agent, benzalkonium chloride) or $Cu_2O/Ti_3C_2T_x$ nanosheets without and with NIR irradiation. Healthy mice took about 14 days to recover,

while a similar-sized wound (10 mm) healed in at least 20 days or more in diabetic db/db mice [68]. Relative wound area on a postoperative day 12 of the $Cu_2O/Ti_3C_2T_x$ nanosheets-treated groups without and with NIR laser irradiation were reduced to ~ 57% and ~ 37%, respectively, ascribing to the effective reduction in bacterial colony count from the wound site when coupled with NIR irradiation (Fig. 6Ab). On the contrary, untreated wounds revealed negligible closure in the wound area and a high population of infected bacteria in the wound sites. Colony formation assay of MRSA collected on postoperative day 14 from wound sites co-treated with $Cu_2O/Ti_3C_2T_x$ nanosheets and NIR laser revealed insignificant bacteria growth (almost no colony formation) when compared to untreated ones (252 ± 14 CFU, $n = 3$) or 3 M treated (234 ± 17 CFU, $n = 3$) and to those treated with nanosheets without NIR irradiation (70 ± 5 CFU, $n = 3$) (Fig. 6Ba). The wound treated with $Cu_2O/Ti_3C_2T_x$ nanosheets under NIR irradiation displayed enhanced antimicrobial activity towards MRSA infected tissues mainly because of the localized photothermal effect (~ 50 °C; Additional file 1: Fig. S15) and high levels of ROS (i.e., $O_2^{\bullet-}$ and H_2O_2) produced in situ (Fig. 6Bb). In addition, the contribution of sharp edges-induced physical disruption of bacterium membrane cannot be excluded. Although the local temperature of ~ 50 °C is relatively higher, the mice can tolerate it for a short period (10 min). The photothermal ablation process can be controlled by adjusting the drug concentration (Additional file 1: Fig. S8A) and power density (Additional file 1: Fig. S8B) of the laser. Minimal damage to the skin cells was observed mainly because dosage (50 μg mL^{-1}) and power density (0.54 W cm^{-2}) employed for wound treatment is optimal for a shorter duration (10 min).

Moreover, histological evaluation of hematoxylin and eosin (H&E)- and Masson's trichrome-stained tissue specimens collected from the infectious site on postoperative day 14, showed that untreated groups displayed a large number of immune cells (black arrow) (Fig. 6C). In chronic wounds, compromised neutrophil and macrophage phagocytosis protract the regeneration of skin fibroblasts, while bacteria consume major amount of complementary proteins. Such processes occur during the inflammatory phase of wound healing, which delays the healing process [69, 70]. Furthermore, less pliable erythrocytes in protracted proliferative phase are unable to deliver oxygen to the wounded site for tissue metabolism and collagen synthesis [71]. Blue color in Masson's trichrome staining represents collagen fibers, and the intensity is attributed to the collagen content in that particular tissue specimens (Fig. 6C). We observed more collagen fiber deposition in the recovered dermal layers, after treatment with $Cu_2O/Ti_3C_2T_x$ nanosheets

Hsu *et al. Journal of Nanobiotechnology* (2022) 20:235

Page 11 of 15

Fig. 6 **Aa** Digital photographs and **b** relative wound closure area, **Ba** representative colony formation assays of MRSA collected from the wound site on day 14, and **b** bacterial viability of MRSA until day 18 from the wounds untreated and treated with 3 M bandage and 50 μg mL^{-1} (in terms of MXene) of Cu$_2$O/Ti$_3$C$_2$T$_x$ nanosheets without and with NIR irradiation (808 nm, 0.54 W cm^{-2}, 10 min). The error bars **b** in **A** and **B** represent the standard deviation of three repeated measurements. **C** Histological analysis of tissue sections isolated on postoperative day 14 from the untreated and treated wounds. Red and yellow lines represent the thickness of the epidermis and dermis, respectively. Scale bar in **A** and **C** are 1 cm and 100 μm, respectively

coupled with NIR irradiation. Efficient antimicrobial response of the Cu$_2$O/Ti$_3$C$_2$T$_x$ nanosheets in the presence of NIR irradiation promoted angiogenesis, epithelialization, and collagen synthesis and formation of blood vessels and hair follicles (blue arrow). The development of new network of blood vessels allows an adequate supply of nutrients and oxygen, which stimulate the growth of granulation tissue. Moreover, we also observed higher degree of epithelialization (green arrow) in the Cu$_2$O/Ti$_3$C$_2$T$_x$ nanosheets treated wounds under NIR irradiation, compared to other groups, implying full recovery of wounds (Fig. 6C).

Discussions

In today's world with fast-developing therapeutic advances, it is vital to investigate new and improved alternative strategies against bacteria and viruses, especially after witnessing the COVID-19 havoc. But with progressing improvements in tackling these issues, the multidrug-resistant bacteria has started to adapt according to conditions resulting in degradation of existing antibiotics and alteration of bacteria efflux pumps posing a severe threat to sustaining human life. To address these issues, numerous research has been actively harnessing the potential of two-dimensional nanomaterials and various carbon-, metal/metal oxide-based structures [10–13]. These materials are often referred to as "endogenous antimicrobial" and damage bacteria through direct contact with bacterium membrane. However, their long-term uses may lead to AMR [17]. On the other hand, the cytotoxicity of metal/metal oxide due to leaching of metal ions cannot be overlooked. This situation lays the foundation for developing bio-compatible nanomaterials capable of in vivo action through multiple routes targeting colossal challenges. The enhanced specific surface area

Hsu *et al. Journal of Nanobiotechnology*   (2022) 20:235

Page 12 of 15

and fast electron transfer ensure sufficient surface-active sites, particularly ultrathin 2D nanomaterials which has also been highlighted in Zhao et al. work using r-GO nanosheets for antimicrobial therapies [20–23]. However, r-GO was inable to provide in-depth tissue penetration or localized thermal effect to inactivate bacteria. Owing to various structural properties, MXene comes to light as a potential candidate [28, 29]. An appreciable amount of work has been going on the heterojunctions and inducing defects in these structures, but the drawback lies in using the aqueous solution with low ionic strength because of poor stability in biologically complex fluids [33]. Our developed $Cu_2O/Ti_3C_2T_x$ nanosheets have several advantages such as facile synthesis $Cu_2O/Ti_3C_2T_x$ nanosheets conducted at room temperature, and as-prepared nanosheets exhibited remarkable biocompatibility mainly due to their high aqueous dispersibility and low toxic natures of Cu and Ti. The $Cu_2O/Ti_3C_2T_x$ nanosheets possess high photo-to-heat conversion efficiency and characteristic NIR absorbance, which allowed the development of a lower energy-based bacterial eradication from infected wounds. Thus they have a great scope as an antimicrobial modality for various biomedical applications.

Conclusions

We demonstrated a self-redox reaction of $CuCl_2$ and $Ti_3C_2T_x$ MXene to form TiO_2 and Cu_2O species in situ on the surfaces of $Ti_3C_2T_x$ nanosheets. Under NIR irradiation, the surface Cu_2O species on $Cu_2O/Ti_3C_2T_x$ nanosheets boost the production of H_2O_2. In addition, temperature rise in response to low energy photons acted as a thermal gradient, which contributed to the production of H_2O_2. The MIC_{90} values of as-prepared $Cu_2O/Ti_3C_2T_x$ nanosheets under NIR irradiation against tested bacteria was > tenfold lower than pristine $Ti_3C_2T_x$ MXene. Broad-spectrum antimicrobial susceptibility to various bacteria, including MDR bacteria, was achieved due to systematically generated therapeutic response, at first, sharp-edges of nanosheets physically attacked bacterium membrane (direct contact-mediated bacterial disintegration), then, NIR irradiation induced localized heat (~ 58 °C, photothermal therapy), and enhanced ROS production (catalytic therapy). The $Cu_2O/Ti_3C_2T_x$ nanosheets showed insignificant cytotoxicity and negligible hemolytic activity against human skin cells (NIH-3T3 skin cells) and RBCs, respectively. In vivo efficacy of $Cu_2O/Ti_3C_2T_x$ nanosheets was proven by treating the MRSA-infected surgical wounds created on diabetic mice under photoirradiation. Topically administered $Cu_2O/Ti_3C_2T_x$ nanosheets efficiently eliminated microbial pathogenesis caused by MRSA to accelerate wound healing via angiogenesis, epithelialization, and

collagen deposition. Intrinsic radical scavenging capabilities of MXene may contribute to accelerated wound healing. Anti-oxidant properties of MXene and the role of Cu_2O in enhanced stimulation of immune cells is currently under investigation. Our developed, $Cu_2O/Ti_3C_2T_x$ nanosheets possess superior biocompatibility, photothermal efficiency, and catalytic properties, which makes them an ideal candidate for the treatment of infectious diseases and wound healing applications.

Methods

Synthesis of MXene and $Cu_2O/Ti_3C_2T_x$ nanosheets

Nanosheets were prepared through a previously reported minimally intensive layer delamination (MILD) method, with minor modifications [34]. 40 mL of HCl (9 M) was added slowly into a PTFE bottle containing 4 g of LiF, which was then stirred for 30 min (600 r.p.m.) at ambient temperature. To which, 4 g of Ti_3AlC_2 MAX powder was slowly added over the course of 30 min. Then, the mixture was heated at 40 °C under constant stirring for 24 h and then subjected to centrifugation at a relative centrifugal force (RCF) of 3000g (10 min, 25 °C) to collect the etched multi-layered MXene in the pellet. The obtained residues were repeatedly washed with ultrapure water until the pH value reached to ~ 6.0. The delamination of purified multi-layered MXene was carried out by probe sonicator (Pulse 150 Ultrasonic Homogenizer, Thomas Scientific, Swedesboro, NJ, USA) in degassed water, under a flow of argon (Ar) gas for 4 h. During sonication, the surrounding temperature was maintained at 4 °C, while the frequency was set to 37 kHz, and the power of amplitude was 80%. The resulting solution was then centrifuged (RCF 3000×g, 5 min, 27 °C) to separate the delaminated flakes (dark green; monolayer $Ti_3C_2T_x$ or MXene) from the unexfoliated sheets and larger particles. The concentration of purified MXene (in terms of mg mL^{-1}) was determined using freeze-drying method. Freshly prepared monolayer MXene (1.0 mg mL^{-1}, 0.5 mL) dispersed in sodium phosphate buffer (20 mM, pH 7.0) was separately incubated with $CuCl_2$ solutions (20, 50, 100, 200 μg mL^{-1}, in terms of Cu; 0.5 mL in water) for 1 h under continuous shaking (100 r.p.m.) at ambient temperature to obtain $Cu_2O/Ti_3C_2T_x$ nanosheets.

Photoresponsive properties of $Cu_2O/Ti_3C_2T_x$ nanosheets

A continuous NIR laser (808 nm) with DPSSL driver II (Tangyu Precision Machinery Industry Co., Ltd., Taipei, Taiwan) was used to evaluate photocatalytic and photothermal performances of nanosheets. Temperature profiles of 50 μg mL^{-1} (in terms of $Ti_3C_2T_x$) of as-prepared $Ti_3C_2T_x$ MXene and $Cu_2O/Ti_3C_2T_x$ MXene dispersed in phosphate-buffered saline (PBS, pH 7.4, containing 137 mM NaCl, 2.7 mM KCl, 10 mM Na_2HPO_4, and

Hsu *et al. Journal of Nanobiotechnology*   (2022) 20:235

Page 13 of 15

2.0 mM KH_2PO_4; 1 mL) solution under NIR laser irradiation (0.54 W cm^{-2}) were continuously recorded using a TFC–305A Type K single input thermocouple thermometer (Yi Chun Electrics Co., Ltd., Taipei, Taiwan) for 10 min.

A freshly prepared Amplex Red (AR; 50 µM) was added into a 1.0 mL vial containing $Ti_3C_2T_x$ or $Cu_2O/Ti_3C_2T_x$ nanosheets (50 µg mL^{-1}; in terms of $Ti_3C_2T_x$) dispersed in PBS solution with horseradish peroxidase (HRP; 0.1 unit mL^{-1}) to estimate the catalytic generation of H_2O_2 [65]. The aliquots were then incubated at 0 °C, 58 °C, and at ambient temperature separately in dark and under NIR irradiation (808 nm, 0.54 W cm^{-2}) for 10 min. Afterwards, the mixtures were subjected to measure the fluorescence intensity at an excitation/emission of 540/590 nm using a monochromatic microplate spectrophotometer (Synergy 4, Biotek Instruments, Winooski, VT, USA). We employed 5,5-dimethyl-1-pyrroline-*N*-oxide (DMPO) as a spin trap to perform Electron Spin Resonance (ESR) spectroscopy analysis for the detection of ROS. The ESR parameters are as follows: microwave power, 15 mW; microwave frequency, 9.8 gHz; scan range, 100 G; time constant, 0.328 s; sampling time, 20 ms; receiver gain, 30; modulation frequency, 100 kHz; g-factor, 2.00627; modulation amplitude, 0.1 mT.

Determination of superoxide free radical

A freshly prepared MTT (1.0 mM) was added into a 1.0 mL vial containing $Cu_2O/Ti_3C_2T_x$ nanosheets (50 µg mL^{-1}; in terms of $Ti_3C_2T_x$) dispersed in PBS solution (pH 7.4) to assess the formation of MTT-formazan in the absence and presence of NIR irradiation (808 nm, 0.54 W cm^{-2}, 10 min). MTT incubated with KO_2 (0.5 mg mL^{-1}) served as a positive control. Afterwards, as obtained purple-colored precipitates were dissolved in 50% isopropanol (1:1) and the absorbance at 576 nm was recorded immediately using a monochromatic microplate spectrophotometer (Synergy 4).

Bacterial growth

Staphylococcus aureus (BCRC10781) and *E. coli* (BRBC 12438) were separately grown in Luria Bertani (LB) media, while MRSA (ATCC 43300) and GREC (BRCG 20703) were cultured individually in 1% penicillin and gentamicin containing LB broth, respectively. A single colony of each strain was plucked from solidified agar plates and inoculated in LB medium (1.0 mL). The cultures were then incubated at 37 °C under continuous shaking (200 r.p.m.), until the absorbance at 600 nm (OD_{600}) reached to 1.0 (optical path length: 1.0 cm). Each of the bacterial suspension was centrifuged (RCF $3000 \times g$, 10 min, 25 °C) and washed thrice with PBS solution. Finally, 100 µL of the *E. coli* suspension [5.0×10^3 colony-forming unit (CFU) mL^{-1}] was spread onto the solidified LB agar plates for the assessment of colony formation assay.

In vitro antibacterial assays

The standard broth microdilution method determined the MIC_{90} (minimal inhibitory concentrations required to kill > 90% of total bacteria population) values against four different bacterial strains. Bacterial suspensions (1.0×10^4 CFU mL^{-1}) were incubated separately with $CuCl_2$, $Ti_3C_2T_x$, or $Cu_2O/Ti_3C_2T_x$ nanosheets in PBS solution (pH 7.4) at 37 °C under continuous shaking (250 r.p.m.) for 1 h and further incubated for 10 min at ambient temperature without and with NIR irradiation (808 nm, 0.54 Wcm^{-2}, 10 min). Then, each of the diluted bacterial mixtures (100 µL) was spread onto the solidified LB agar plates, and CFUs were counted manually after 24 h incubation at 37 °C.

Treatment of infected wounds using $Cu_2O/Ti_3C_2T_x$ nanosheets

The in vivo eradication of MRSA by $Cu_2O/Ti_3C_2T_x$ nanosheets was demonstrated using BKS Cg–Dock7^m+/+Leprdb/J (db/db) male mice (5–6 weeks old, weighing 35–45 g). All animal experiments were conducted in accordance with the institutional guidelines of Care and Use of Laboratory Animals of National Taiwan University and granted by the Institutional Animal Care and Use Committee of the National Laboratory Animal Center, Taipei, Taiwan (IACUC Approval No. IACUC2012-037). The mice were anesthetized using a mixture of xylazine (117 mg kg^{-1}) and Zoletil (5 mg kg^{-1}). After shaving the dorsal skin of mice, the skin was disinfected using 70% ethyl alcohol (v/v) before aseptic surgery. An incision created circular wounds of ~ 10 mm in diameter on the skin of each mouse with a sterile stainless-surgical scissors. Microbial infection was induced by incubating the MRSA suspensions (1×10^8 CFU mL^{-1}; 50 µL) onto the wound site for 6 h. 14 days post-surgery, the wound sites were swabbed using a sterile cotton swab and cultured on LB agar plates for 24 h at 37 °C to confirm the MRSA infection. Then, $Cu_2O/MXene$ nanosheets were topically administered onto the wound site under NIR laser irradiation (808 nm, 0.54 W cm^{-2}, 5 min; every other day). To evaluate the in vivo antimicrobial activity of as-prepared $Cu_2O/MXene$ nanosheets, tissue fluid (~ 10 µL) was swabbed from infectious wound site untreated and treated with $Cu_2O/Ti_3C_2T_x$ nanosheets without or with NIR laser irradiation on day 0, 2, 4, 6, 8, 10, 12, 14, 16, and 18 and separately grown on the LB agar plates to monitor the bacteria growth through colony formation assay. Photographs of the wound area were captured using a digital camera to observe the real-time

Hsu *et al. Journal of Nanobiotechnology*   (2022) 20:235

Page 14 of 15

progress of the infected wounds. Tissue sections containing the entire wound including surrounding healthy skin (dermis and subcutaneous tissue) were surgically removed on postoperative day 14 for histological evaluation. Collagen formation and skin histology of wounded tissue were studied by Masson's trichrome and Hematoxylin and eosin (H&E) staining, respectively.

Supplementary Information

The online version contains supplementary material available at https://doi.org/10.1186/s12951-022-01428-3.

Additional file 1. Additional methods, figures and tables.

Declarations

Consent for publication
All authors agree to be published.

Competing interests
The authors have declared that no competing interest exists.

Author details
[1]Department of Chemistry, National Taiwan University, Taipei 10617, Taiwan. [2]School of Basic Sciences, Indian Institute of Technology, Kamand campus, Mandi, Himachal Pradesh 175005, India. [3]Institute of Analytical and Environmental Sciences, National Tsing Hua University, Hsinchu 30013, Taiwan. [4]Department of Bioscience and Biotechnology and Center of Excellence for the Oceans, National Taiwan Ocean University, Keelung 202301, Taiwan. [5]School of Pharmacy, College of Pharmacy, Kaohsiung Medical University, Kaohsiung 80708, Taiwan.

References
1. Bloom DE, Cadarette D. Infectious disease threats in the twenty-first century: strengthening the global response. Front Immunol. 2019;10:549.
2. Toner E, Adlja A, Gronvall GK, Cicero A, Inglesby TV. Antimicrobial resistance is a global health emergency. Health Secur. 2015;13:153–5.
3. Afonso AC, Oliveira D, Saavedra MJ, Borges A, Simões M. Biofilms in diabetic foot ulcers: impact, risk factors and control strategies. Int J Mol Sci. 2021;22:8278.
4. Kohanski MA, Dwyer DJ, Collins JJ. How antibiotics kill bacteria: from targets to networks. Nat Rev Microbiol. 2010;8:423–35.
5. Fischbach MA, Walsh CT. Antibiotics for emerging pathogens. Science. 2009;325:1089–93.
6. Tyers M, Wright GD. Drug combinations: a strategy to extend the life of antibiotics in the 21st century. Nat Rev Microbiol. 2019;17:141–55.
7. Crofts TS, Gasparrini AJ, Dantas G. Next-generation approaches to understand and combat the antibiotic resistome. Nat Rev Microbiol. 2017;15:422–34.
8. de Kraker MEA, Stewardson AJ, Harbarth S. Will 10 million people die a year due to antimicrobial resistance by 2050? PLoS Med. 2016;13:e1002184.
9. Blair JMA, Webber MA, Baylay AJ, Ogbolu DO, Piddock LJV. Molecular mechanisms of antibiotic resistance. Nat Rev Microbiol. 2015;13:42–51.
10. Anand A, Unnikrishnan B, Wei SC, Chou CP, Zhang LZ, Huang CC. Graphene oxide and carbon dots as broad-spectrum antimicrobial agents-a minireview. Nanoscale Horiz. 2019;4:117–37.
11. Gupta A, Mumtaz S, Li C-H, Hussain I, Rotello VM. Combatting antibiotic-resistant bacteria using nanomaterials. Chem Soc Rev. 2019;48:415–27.
12. Wang L, Hu C, Shao L. The antimicrobial activity of nanoparticles: present situation and prospects for the future. Int J Nanomed. 2017;12:1227.
13. Zheng K, Xie J. Cluster materials as traceable antibacterial agents. Acc Mater Res. 2021;2:1104–16.
14. Nain A, Tseng YT, Wei SC, Periasamy AP, Huang CC, Tseng FG, et al. Capping 1,3-propanedithiol to boost the antibacterial activity of protein-templated copper nanoclusters. Nanoscale. 2020;389: 121821.
15. Vincent M, Duval RE, Hartemann P, Engels-Deutsch M. Contact killing and antimicrobial properties of copper. J Appl Microbiol. 2018;124:1032–46.
16. Wang Y, Yang Y, Shi Y, Song H, Yu C. Antibiotic-free antibacterial strategies enabled by nanomaterials: progress and perspectives. Adv Mater. 2020;32:1904106.
17. Shaikh S, Nazam N, Rizvi SMD, Ahmad K, Baig MH, Lee EJ, et al. Mechanistic insights into the antimicrobial actions of metallic nanoparticles and their implications for multidrug resistance. Int J Mol Sci. 2019;20:2468.
18. Bondarenko O, Juganson K. Toxicity of Ag, CuO and ZnO nanoparticles to selected environmentally relevant test organisms and mammalian cells in vitro: a critical review. Arch Toxicol. 2013;87:1181–200.
19. Le Ouay B, Stellacci F. Antibacterial activity of silver nanoparticles: a surface science insight. Nano Today. 2015;10:339–54.
20. Dwivedi N, Dhand C, Kumar P, Srivastava AK. Emergent 2D materials for combating infectious diseases: the potential of MXenes and MXene–graphene composites to fight against pandemics. Mater Adv. 2021;2:2892–905.
21. Sun W, Wu F. Two-dimensional materials for antimicrobial applications: graphene materials and beyond. Chem Asian J. 2018;13:3378–410.
22. Begum S, Pramanik A, Davis D, Patibandla S, Gates K, Gao Y, et al. 2D and heterostructure nanomaterial based strategies for combating drug-resistant bacteria. ACS Omega. 2020;5:3116–30.
23. Nanobiotechnol J, Zhao B, Wang H, Dong W, Cheng S, Li H, et al. A multifunctional platform with single-NIR-laser-triggered photothermal and NO release for synergistic therapy against multidrug-resistant Gram-negative bacteria and their biofilms. J Nanobiotechnol. 2020;18:1–25.
24. Ding H, Han D, Han Y, Liang Y, Liu X, Li Z. Visible light responsive CuS/protonated g-C$_3$N$_4$ heterostructure for rapid sterilization. J Hazard Mater. 2020;393: 122423.
25. Naguib M, Barsoum MW, Gogotsi Y. Ten years of progress in the synthesis and development of MXenes. Adv Mater. 2021;33:2103393.
26. Meng W, Liu X, Song H, Xie Y, Shi X, Dargusch M, et al. Advances and challenges in 2D MXenes: from structures to energy storage and conversions. Nano Today. 2021;40: 101273.
27. Wei Y, Zhang P, Soomro RA, Zhu Q, Xu B. Advances in the synthesis of 2D Mxenes. Adv Mater. 2021;33:2103148.
28. Lin H, Chen Y, Shi J. Insights into 2D MXenes for versatile biomedical applications: current advances and challenges ahead. Adv Sci. 2018;5:1800518.

Hsu *et al. Journal of Nanobiotechnology* (2022) 20:235

Page 15 of 15

29. Huang K, Li Z, Lin J, Han G, Huang P. Two-dimensional transition metal carbides and nitrides (MXenes) for biomedical applications. Chem Soc Rev. 2018;47:5109–24.

30. Rasool K, Mahmoud KA, Johnson DJ, Helal M, Berdiyorov GR, Gogotsi Y. Efficient antibacterial membrane based on two-dimensional $Ti_3C_2T_x$ (MXene) nanosheets. Sci Rep. 2017;7:1–11.

31. Arabi Shamsabadi A, Sharifian GhM, Anasori B, Soroush M. Antimicrobial mode-of-action of colloidal $Ti_3C_2T_x$ MXene nanosheets. ACS Sustain Chem Eng. 2018;6:16586–96.

32. Li J, Li Z, Liu X, Li C, Zheng Y, Yeung KWK, et al. Interfacial engineering of $Bi_2S_3/Ti_3C_2T_x$ MXene based on work function for rapid photo-excited bacteria-killing. Nat Commun. 2021;12:1–10.

33. Zheng K, Li S, Jing L, Chen P, Xie J. Synergistic antimicrobial titanium carbide (MXene) conjugated with gold nanoclusters. Adv Healthc Mater. 2020;9:2001007.

34. Wu C-W, Unnikrishnan B, Chen I-WP, Harroun SG, Chang H-T, Huang C-C. Excellent oxidation resistive MXene aqueous ink for micro-supercapacitor application. Energy Storage Mater. 2020;25:563–71.

35. Hou T, Wang B, Ma M, Feng A, Huang Z, Zhang Y, et al. Preparation of two-dimensional titanium carbide ($Ti_3C_2T_x$) and $NiCo_2O_4$ composites to achieve excellent microwave absorption properties. Compos Part B Eng. 2020;180: 107577.

36. Wu X, Wang Z, Yu M, Xiu L, Qiu J. Stabilizing the MXenes by carbon nano-plating for developing hierarchical nanohybrids with efficient lithium storage and hydrogen evolution capability. Adv Mater. 2017;29:1607017.

37. Zhang M, Chen X, Sui J, Abraha BS, Li Y, Peng W, et al. Improving the performance of a titanium carbide MXene in supercapacitors by partial oxidation treatment. Inorg Chem Front. 2020;7:1205–11.

38. Wang Z, Xu Z, Huang H, Chu X, Xie Y, Xiong D, et al. Unraveling and regu-lating self-discharge behavior of $Ti_3C_2T_x$ MXene-based supercapacitors. ACS Nano. 2020;14:4916–24.

39. She H, Zhou H, Li L, Zhao Z, Jiang M, Huang J, et al. Construction of a two-dimensional composite derived from TiO_2 and SnS_2 for enhanced photo-catalytic reduction of CO_2 into CH_4. ACS Sustain Chem Eng. 2018;7:650–9.

40. Zhang CJ, Pinilla S, McEvoy N, Cullen CP, Anasori B, Long E, et al. Oxidation stability of colloidal two-dimensional titanium carbides (MXenes). Chem Mater. 2017;29:4848–56.

41. Guo Z, Gao L, Xu Z, Teo S, Zhang C, Kamata Y, et al. High electrical conductiv-ity 2D MXene serves as additive of perovskite for efficient solar cells. Small. 2018;14:1802738.

42. Xu H, Ren A, Wu J, Wang Z. Recent advances in 2D MXenes for photodetec-tion. Adv Funct Mater. 2020;30:2000907.

43. Chen G, Wang H, Wei X, Wu Y, Gu W, Hu L, et al. Efficient Z-Scheme het-erostructure based on $TiO_2/Ti_3C_2T_x/Cu_2O$ to boost photoelectrochemical response for ultrasensitive biosensing. Sensors Actuators B Chem. 2020;312: 127951.

44. Cai T, Wang L, Liu Y, Zhang S, Dong W, Chen H, et al. Ag_3PO_4/Ti_3C_2 MXene inter-face materials as a Schottky catalyst with enhanced photocatalytic activities and anti-photocorrosion performance. Appl Catal B Environ. 2018;239:545–54.

45. Nain A, Tseng YT, Gupta A, Lin YF, Sangili A, Huang YF, et al. Anti-microbial/ oxidative/inflammatory nanogels accelerate chronic wound healing. Smart Mater Med. 2022. https://doi.org/10.1016/j.smaim.2021.12.006.

46. Mishin V, Gray JP, Heck DE, Laskin DL, Laskin JD. Application of the Amplex red/ horseradish peroxidase assay to measure hydrogen peroxide generation by recombinant microsomal enzymes. Free Radic Biol Med. 2010;48:1485–91.

47. Zhang S, Cao C, Lv X, Dai H, Zhong Z, Liang C, et al. A H_2O_2 self-sufficient nano-platform with domino effects for thermal-responsive enhanced chemody-namic therapy. Chem Sci. 2020;11:1926–34.

48. Dvoranová D, Barbieriková Z, Brezová V. Radical intermediates in pho-toinduced reactions on TiO_2 (an EPR spin trapping study). Molecules. 2014;19:17279–304.

49. Deng L, Sheng D, Liu M, Yang L, Ran H, Li P, et al. A near-infrared laser and H_2O_2 activated bio-nanoreactor for enhanced photodynamic therapy of hypoxic tumors. Biomater Sci. 2020;8:858–70.

50. Wang H, Cheng H, Wang F, Wei D, Wang X. An improved 3-(4, 5-dimeth-ylthiazol-2-yl)-2, 5-diphenyl tetrazolium bromide (MTT) reduction assay for evaluating the viability of *Escherichia coli* cells. J Microbiol Methods. 2010;82:330–3.

51. Zhao Y, Zhang S, Shi R, Waterhouse GIN, Tang J, Zhang T. Two-dimensional photocatalyst design: a critical review of recent experimental and computa-tional advances. Mater Today. 2020;34:78–91.

52. Zhang Y, Xia W, Wu Y, Zhang P. Prediction of MXene based 2D tunable band gap semiconductors: GW quasiparticle calculations. Nanoscale. 2019;11:3993–4000.

53. Akhtar N, Rani M, Mahmood A, Saba H, Khan S, Murtaza G, et al. Synthesis and characterization of MXene/$BiCr_2O_4$ nanocomposite with excellent electro-chemical properties. J Mater Res Technol. 2021;15:2007–15.

54. Liu T, Xiao B, Xiang F, Tan J, Chen Z, Zhang X, et al. Ultrasmall copper-based nanoparticles for reactive oxygen species scavenging and alleviation of inflammation related diseases. Nat Commun. 2020;11:1–16.

55. Wang W, Feng H, Liu J, Zhang M, Liu S, Feng C, et al. A photo catalyst of cuprous oxide anchored MXene nanosheet for dramatic enhancement of synergistic antibacterial ability. Chem Eng J. 2020;386: 124116.

56. Xu D, Li Z, Li L, Wang J. Insights into the photothermal conversion of 2D MXene nanomaterials: synthesis, mechanism, and applications. Adv Funct Mater. 2020;30:2000712.

57. Hu W, Miao X, Tao H, Baev A, Ren C, Fan Q, et al. Manipulating nonradiative decay channel by intermolecular charge transfer for exceptionally improved photothermal conversion. ACS Nano. 2019;13:12006–14.

58. Han X, Huang J, Lin H, Wang Z, Li P, Chen Y. 2D ultrathin MXene-based drug-delivery nanoplatform for synergistic photothermal ablation and chemother-apy of cancer. Adv Healthc Mater. 2018. https://doi.org/10.1002/adhm.20170 1394.

59. Li R, Zhang L, Shi L, Wang P. MXene Ti_3C_2: an effective 2D light-to-heat conver-sion material. ACS Nano. 2017;11:3752–9.

60. Boerigter C, Campana R, Morabito M, Linic S. Evidence and implications of direct charge excitation as the dominant mechanism in plasmon-mediated photocatalysis. Nat Commun. 2016;7:1–9.

61. Shi Y, Cui D, Zhang Z. Quantitative study of the nonlinearly enhanced pho-toacoustic/ photothermal effect by strong LSPR-coupled nanoassemblies. Nanomaterials. 2020;10:1942.

62. Liu Y, Tian Y, Han Q, Yin J, Zhang J, Yu Y, et al. Synergism of 2D/1D MXene/ cobalt nanowire heterojunctions for boosted photo-activated antibacte-rial application. Chem Eng J. 2021;410: 128209.

63. Wang D, Fang Y, Yu W, Wang L, Xie H, Yue Y. Significant solar energy absorption of MXene $Ti_3C_2T_x$ nanofluids via localized surface plasmon resonance. Sol Energy Mater Sol Cells. 2021;220: 110850.

64. Wiegand I, Hilpert K, Hancock REW. Agar and broth dilution methods to determine the minimal inhibitory concentration (MIC) of antimicrobial substances. Nat Protoc. 2008;3:163–75.

65. Nain A, Wei SC, Lin YF, Tseng YT, Mandal RP, Huang YF, et al. Copper sulfide nanoassemblies for catalytic and photoresponsive eradication of bacteria from infected wounds. ACS Appl Mater Interfaces. 2021;13:7865–78.

66. Hudson MA, Siegele DA, Lockless SW. Use of a fluorescence-based assay to measure *Escherichia coli* membrane potential changes in high throughput. Antimicrob Agents Chemother. 2020;64:e00910-e920.

67. Parastan R, Kargar M, Solhjoo K, Kafilzadeh F. *Staphylococcus aureus* biofilms: structures, antibiotic resistance, inhibition, and vaccines. Gene Reports. 2020;20: 100739.

68. Ishida Y, Kuninaka Y, Nosaka M, Furuta M, Kimura A, Taruya A, et al. CCL2-mediated reversal of impaired skin wound healing in diabetic mice by normalization of neovascularization and collagen accumulation. J Invest Dermatol. 2019;139:2517–27.

69. Banerjee K, Madhyastha R, Nakajima Y, Maruyama M, Madhyastha H. Nanoceutical adjuvants as wound healing material: precepts and pros-pects. Int J Mol Sci. 2021;22:4748.

70. Landén NX, Li D, Ståhle M. Transition from inflammation to proliferation: a critical step during wound healing. Cell Mol Life Sci. 2016;73:3861–85.

71. Nain A, Huang HH, Chevrier DM, Tseng YT, Sangili A, Lin YF, et al. Catalytic and photoresponsive bismuth-doped copper sulfide nanocomposites with multiple heterojunctions and surface vacancies for the treatment of multidrug-resistant clinical biofilm-associated infections. Nanoscale. 2021;13:18632–46.

Publisher's Note